

## ARTICLE

## OPEN



# Robust behavior and spin-texture stability of the topological surface state in $\text{Bi}_2\text{Se}_3$ upon deposition of gold

O. J. Clark<sup>1</sup>, F. Freyse<sup>1,2</sup>, L. V. Yashina<sup>1</sup>, O. Rader<sup>1</sup> and J. Sánchez-Barriga<sup>1</sup>✉

The Dirac point of a topological surface state (TSS) is protected against gapping by time-reversal symmetry. Conventional wisdom stipulates, therefore, that only through magnetisation may a TSS become gapped. However, non-magnetic gaps have now been demonstrated in  $\text{Bi}_2\text{Se}_3$  systems doped with Mn or In, explained by hybridisation of the Dirac cone with induced impurity resonances. Recent photoemission experiments suggest that an analogous mechanism applies even when  $\text{Bi}_2\text{Se}_3$  is surface dosed with Au. Here, we perform a systematic spin- and angle-resolved photoemission study of Au-dosed  $\text{Bi}_2\text{Se}_3$ . Although there are experimental conditions wherein the TSS appears gapped due to unfavourable photoemission matrix elements, our photon-energy-dependent spectra unambiguously demonstrate the robustness of the Dirac cone against high Au coverage. We further show how the spin textures of the TSS and its accompanying surface resonances remain qualitatively unchanged following Au deposition, and discuss the mechanism underlying the suppression of the spectral weight.

*npj Quantum Materials* (2022) 7:36; <https://doi.org/10.1038/s41535-022-00443-9>

## INTRODUCTION

$\text{Bi}_2\text{Se}_3$  and the wider class of Bi and Sb chalcogenides are among the most widely studied topologically non-trivial compounds<sup>1</sup>. A high spin-orbit interaction strength drives a hybridisation and subsequent inversion between the Bi/Sb-*p* derived conduction bands and the chalcogen-*p* derived valence bands near the bulk  $\Gamma$  point. This stabilises a topological surface state (TSS) at  $\bar{\Gamma}$  on the surface, with an (anti-) clockwise rotating chiral spin texture (below) above the Dirac point<sup>1</sup>. As in all strong topological insulators, the bulk-boundary correspondence ensuring the existence of the TSS offers it protection against disorder<sup>2–4</sup>, and, in the presence of time-reversal symmetry (and well-separated top and bottom surfaces<sup>5</sup>), the surface Dirac cone was thought impossible to gap without perturbing the bulk band structure in such a way that causes unwinding of the underlying band inversion<sup>6,7</sup>.

Several studies have investigated the influence of time-reversal symmetry breaking (TRSB) on the topological surface state in  $\text{Bi}_2\text{Se}_3$ . Most effort has been channeled into local TRSB via the inclusion of magnetic impurities. Deposition of Mn, Fe, Co, Ni and Gd on the surface of  $\text{Bi}_2\text{Se}_3$  have each in turn been shown to generate a magnetic field insufficient in strength or shape to induce a gap at the Dirac point of the TSS<sup>3,8–12</sup>. However, the inclusion of magnetic impurities in the material bulk has been demonstrated to destroy the Dirac point and create sizable band gaps in the TSS of 75–200 meV when one of Cr, Mn or Fe are included<sup>6,7,12,13</sup>.

Strikingly, several of these induced band gaps are thought not to be related to any induced long-range magnetic order, as evidenced by the lack of temperature dependence on the size of the gap, at least up to  $\approx 300$  K, a temperature several times larger than the few tens of K transition temperatures where long-range magnetic order would be expected to emerge<sup>12,13</sup>. Instead, for the case of Cr, a superparamagnetic state composed of independent ferromagnetic multimers of several aggregated Cr atoms occupying Bi sites was found sufficient to gap the TSS, despite the lack of long-range ferromagnetic order<sup>13</sup>. Rather differently for the case of Mn, impurity induced resonance states were shown to lift the

topological protection on a local scale, sufficient to observe large band gaps in photoemission experiments originating from hybridisation of the TSS with the near- $E_F$  impurity states<sup>12,14–16</sup>. This entirely non-magnetic mechanism was further verified by the recreation of sizable gaps in the TSS following In doping on concentrations less than that required to drive the system out of the topologically non-trivial regime<sup>12,17</sup>.

Sister compound  $\text{Bi}_2\text{Te}_3$  is almost identical to  $\text{Bi}_2\text{Se}_3$  other than the slightly larger chalcogen derived spin-orbit coupling (SOC) strength. However, although the opening of magnetic gaps is possible<sup>18–21</sup>, the TSS in  $\text{Bi}_2\text{Te}_3$  has so far been found to be resilient against gapping of a non-magnetic origin, with no gap observed via angle-resolved photoemission following bulk Mn doping except below the Curie temperature<sup>18,22–24</sup>, as also shown for  $\text{MnSb}_2\text{Te}_4$ <sup>25</sup>. This suggests a delicate balance between the SOC strength of the constituent atoms contributing the band inversion to the electronic structure, and the ability to induce non-magnetic band gaps in the Dirac points of the topological surface states. However, the question of exactly what the minimal set of prerequisites is for non-magnetic gap opening in these topological surface states remains open. Furthermore, it has been noted that the impurity resonances themselves can completely fill an induced TSS gap<sup>12,26</sup>, possibly helping to reconcile the somewhat contradictory conclusions about the presence of non-magnetic gaps across the range of Bi/Sb calcogenides following the inclusion of magnetic bulk dopants.

Most recently, the picture was further complicated with the TSS in  $\text{Bi}_2\text{Se}_3$  observed to gap significantly following surface deposition of gold by angle-resolved photoemission (ARPES)<sup>27</sup>. While non-magnetic gaps were induced by bulk doping with In<sup>12,23</sup>, this marked the first observation of non-magnetic gaps being driven following surface deposition of a non-magnetic element<sup>27</sup>. The observation was attributed to the formation of an impurity state conjured by the partial substitution of the top-most layer of Bi with Au atoms. The hybridisation between the Au *d* states near the Fermi level ( $E_F$ ) and the TSS is then argued to result in a gapped system, in analogy to the local topological protection lifting in the

<sup>1</sup>Helmholtz-Zentrum Berlin für Materialien und Energie, Elektronenspeicherring BESSY II, Albert-Einstein-Str. 15, 12489 Berlin, Germany. <sup>2</sup>Institut für Physik und Astronomie, Universität Potsdam, Karl-Liebknecht-Str. 24/25, 14476 Potsdam, Germany. ✉email: jaime.sanchez-barriga@helmholtz-berlin.de

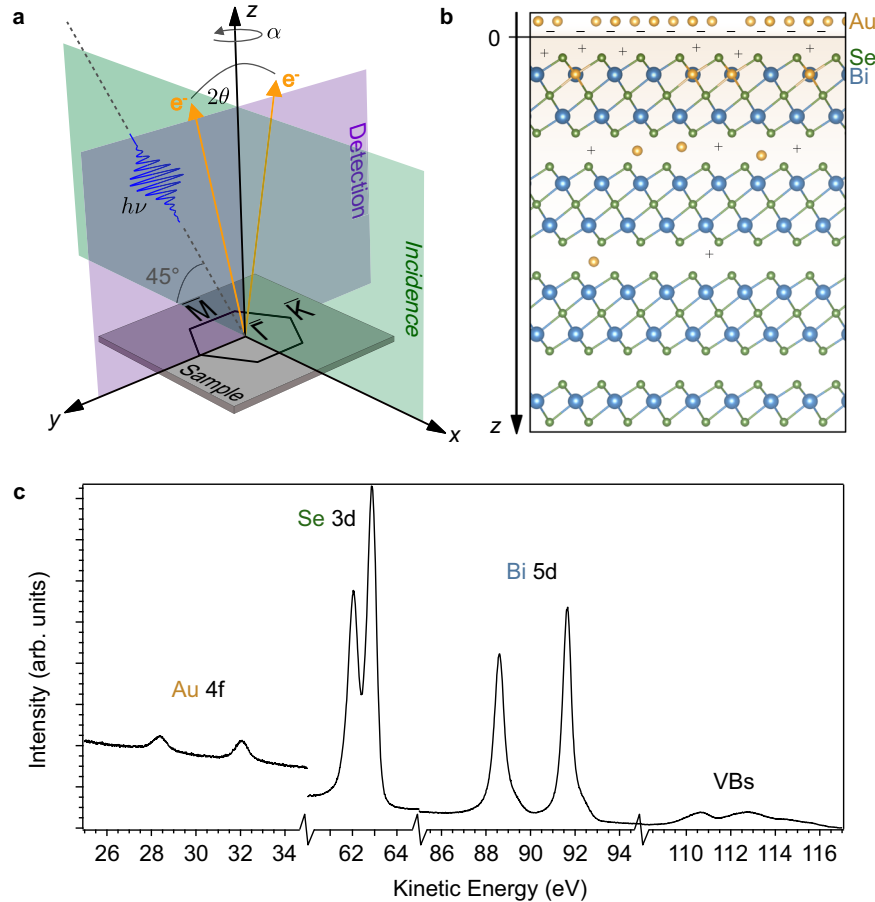


**Fig. 1 Experimental geometry and effects of surface Au deposition.** **a** Experimental geometry of the photoemission experiment.  $\alpha$  and  $\theta$  are the azimuthal and emission (parallel to the analyser slit) angles respectively. **b** Illustration of the  $\text{Bi}_2\text{Se}_3$  system following Au deposition, as viewed along the  $a$ -axis. The sample is cleaved perpendicular to the  $c$ -axis. **c** Wide-energy range angle-integrated spectrum of  $\text{Bi}_2\text{Se}_3$  following 1 ML Au deposition. The incident photon energy was  $h\nu = 120$  eV. Core level states and valence bands (VBs) are labelled.

Mn/In bulk doping scenario<sup>12</sup>. The previous ARPES studies concerning Au-dosed  $\text{Bi}_2\text{Se}_3$  utilised a combination of two fixed energy light sources; a plasma discharge HeI lamp able to provide photons at 21.2 eV, and a 6 eV laser source. Although accompanying band structure calculations presented in refs. <sup>27,28</sup> do seem to well replicate the experimental picture when modelling  $\text{Bi}_2\text{Se}_3$  with a homogenous distribution of Au occupying Bi sites in the first quintile layer, a simple suppression of a photon-energy-dependent photoemission matrix elements has not been ruled out as the cause of the apparent absence of the Dirac point.

In this work, we perform a systematic spin- and angle-resolved photoemission (spin-ARPES) study on  $\text{Bi}_2\text{Se}_3$  single crystals before and after surface Au deposition using a synchrotron light source. We find that the signatures of the TSS Dirac point can become suppressed following Au deposition under certain conditions. However, by changing the incident photon energy the signatures of the Dirac point are fully restored. Therefore, the TSS is robust against Au surface deposition, in contrast to previous works<sup>27,28</sup>. Furthermore, we show that the spin texture obtained in ref. <sup>27</sup> is consistent with a suppressed TSS when paired with the surface resonance states that are well established to accompany the TSS in the pristine compound<sup>29–31</sup>.

## RESULTS AND DISCUSSION

### Effect of Au incorporation on the $\text{Bi}_2\text{Se}_3$ surface

Figure 1b illustrates the role of Au atoms on the surface of single-crystal  $\text{Bi}_2\text{Se}_3$ . The effect of the Au atoms is potentially threefold.

Firstly, while Au can act as a  $p$  or  $n$  dopant<sup>32</sup>, in this system Au lightly  $p$ -dopes the system, causing a band bending effect of the surface layers<sup>27</sup>. In photoemission spectra, this acts to shift bands to shallower binding energies, and, depending on the depth of the confining potential, may allow for the formation of one or more surface-localised quantised sub-bands originating from the bulk valence bands<sup>33–37</sup>. Secondly, the Au atoms can become substitutional defects in near-surface Bi atom sites<sup>27,28</sup>. With enough such substitutions, the formation of Au-derived bands can appear in ARPES spectrum, and this indeed was thought to be the cause of the hybridisation and subsequent gapping of the TSS in ref. <sup>27</sup>. We note that AuSe adsorption formed following a surface reaction has been suggested as an alternate origin of the Au impurity band formation in  $\text{Bi}_2\text{Se}_3$ <sup>38</sup>, although band structure calculations suggest that the former explanation is likely more applicable here<sup>28</sup>. Finally, Au atoms can intercalate within the van der Waals gaps separating  $\text{Bi}_2\text{Se}_3$  layers. This final mechanism is one possible route towards a non-magnetic gapping of a TSS, if the intercalation is sufficient to drive wavefunction overlap of the TSS on the top and newly formed bottom surface, although this too is thought to be unlikely here<sup>12</sup>. Determining the relative effectiveness of these mechanisms is not straightforward, but one can reproduce the same experimental conditions with a controlled sample temperature and careful calibration of a Au source. It is important to note that angle-resolved photoemission is a surface-sensitive technique, with only the top few monolayers of the sample effectively probed. The modification of the near-surface

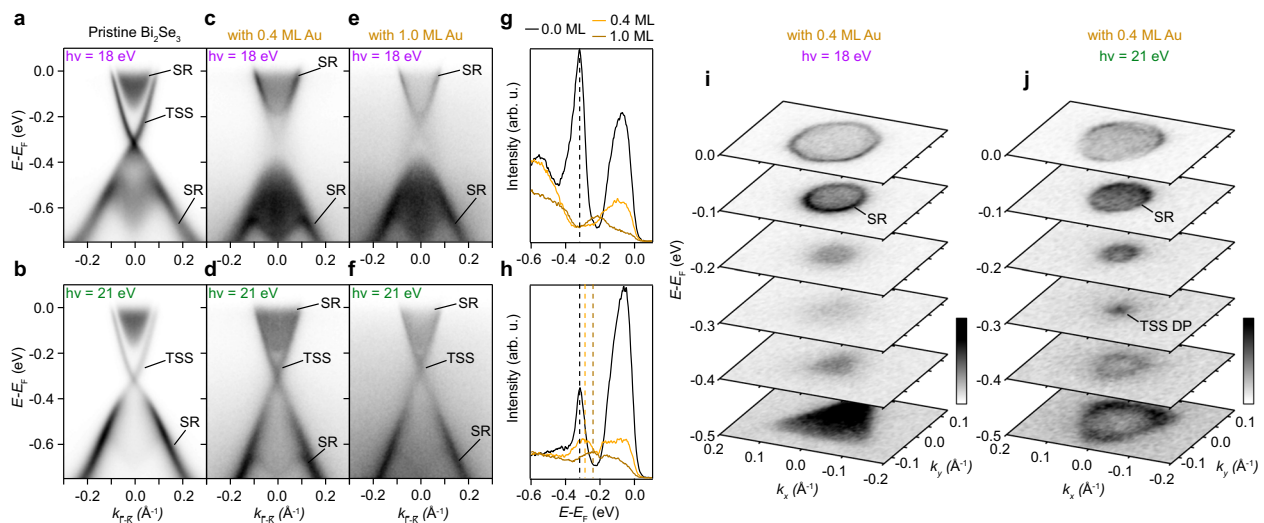


**Fig. 2 Evolution of photoemission spectra following Au deposition.** **a–f** Series of band dispersions of  $\text{Bi}_2\text{Se}_3$  along the  $\bar{\Gamma} - \bar{K}$  direction following various levels of Au surface deposition [**a**, **b** Pristine, **c**, **d** 0.4 monolayer (ML), **e**, **f** 1.0 ML]. **g**, **h** Energy-distribution curves (EDCs) through the  $\bar{\Gamma}$  point for each deposition level. Dashed lines indicate the position of the Dirac point (DP) where applicable. The spectra in the top row (**a**, **c**, **e**, **g**) are taken with 18 eV incident photons and the spectra in the bottom row (**b**, **d**, **f**, **h**) are taken with 21 eV photons. Topological surface state (TSS) and surface resonances (SR) are labelled. **i**, **j** Constant energy  $k_x - k_y$  contours for **i** 18 eV and **j** 21 eV photons following 0.4 ML of Au deposition. Colour scales for photoemission intensity run from low (white) to high (black).

via any combination of the above mechanisms is often a sufficient criterion with which to alter photoemission matrix elements<sup>39</sup>.

Figure 1c shows a typical angle-integrated wide-energy overview of the core level states following a typical Au deposition (here 1.0 ML), which confirms the altered chemical environment imposed by the incorporation of Au. The Au 4f states are clearly seen, while the Se 3d doublet and Bi 5d states remain sharp, but with clear shoulder features on the latter likely due to the presence of multiple Bi valences in the near-surface region.

#### Apparent gapping of the Dirac point upon surface dosing

Figure 2 outlines the effects of Au deposition on the photon-energy-dependent valence electronic structure, and specifically the changes imposed on the topological surface state. First, we review the near- $E_F$  band dispersions for the pristine compound prior to surface deposition. For both 18 and 21 eV photons, the TSS is clearly seen along with the characteristic, ungapped Dirac point. In the former case, the spectral weight of the TSS is higher relative to that of the bulk bands, which disperse somewhat in  $k_z$  between the two spectra. Also present are enhanced sharp regions of spectral weight following the lower perimeters of the  $k_z$ -projected bulk manifolds of both the conduction and valence bands. These too are more clearly seen when using 18 eV photons. We attribute these states to be previously identified spin-polarised surface resonance (SR) states<sup>29–31,40</sup>, and not the surface-localised, near spin-degenerate two-dimensional electron gas (2DEG) previously predicted to exist at the surface of *n*-doped  $\text{Bi}_2\text{Se}_3$ <sup>41</sup>. Like the TSS, the origin of the SR states can be explained by the SOC-driven band inversion, and they too have a predominantly in-plane chiral momentum-locked spin texture. Crucially, however, the sense of chirality of the surface resonance states is opposite to that of the TSS, providing a convenient method by which the states can be distinguished<sup>29–31</sup>.

Following a modest Au deposition of 0.4 ML (Fig. 2c, d), the picture changes substantially. For 18 eV photons, the signatures of the TSS appear to vanish entirely, with a large bandgap of  $\approx 200$  meV separating the bulk conduction and valence bands. This finding, when taken in isolation, is entirely in line with the spectra presented in ref. <sup>27</sup>, in which a similar observation was attributed to being a true gapping of the topological state stemming from the formation

of a Au-derived impurity band. Indeed, we note that the Fermi wave vector of the diffuse bulk conduction band spectral weight appears to increase despite the *p*-doping of the system, likely signalling the formation of Au impurity states near  $E_F$ . However, if the Dirac point of the TSS was indeed destroyed, then there should be no experimental conditions wherein signatures of the Dirac point can be recovered. However, simply by changing the incident photon energy to  $h\nu = 21 \text{ eV}$ , the Dirac point appears intense and sharp. This is in stark contrast to the impurity resonance mechanism proposed previously<sup>27</sup>, in that it suggests the Dirac point is not destroyed at all. Figure 2i, j displays a series of constant energy contours following this deposition step for 18 eV and 21 eV, further confirming the apparent gapping and reforming of the Dirac point with changing photon energy. It seems, therefore, that a photon-energy-dependent matrix element is responsible for the apparent gapping in the present experiment. i.e. the induced gap is not a ground state property of Au-dosed  $\text{Bi}_2\text{Se}_3$ .

We note that the data using  $h\nu = 21 \text{ eV}$  in Fig. 2d, h were collected at an earlier time than the equivalent datasets at  $h\nu = 18 \text{ eV}$  (Fig. 2c, g), and from the same region of the sample, ruling out both a depleting Au retention and non-uniform spatial coverage as explanations for the recovery of the TSS. A change of incident photon energy alters the effective surface sensitivity of the experiment<sup>39</sup>. Therefore, if the topological interface is shifted further into the bulk, separating the topologically non-trivial  $\text{Bi}_2\text{Se}_3$  from the topologically trivial Au layer and vacuum region, then one may expect the higher photon energy to be more capable of probing the interface state (i.e. the TSS). However, the difference in the electron mean free path for 18 and 21 eV is negligible, and a gapping is also seen with an incident photon energy of 6 eV<sup>27</sup>, which results in a larger mean free path than either 18 eV or 21 eV photons<sup>39</sup>.

The remaining reconciling scenario between the data in Fig. 2 and those presented in previous studies, is that there is both a matrix element suppression of the Dirac point for some choices of photon energy following a small amount of surface Au deposition, possibly with a true gapping occurring for more excessive Au depositions. To rule out this explanation, in Fig. 2e, f, we show the same sample with a further 0.6 ML of deposited Au (1.0 ML total). Qualitatively the picture does not change. The sample is more *p*-doped after the second deposition step as seen from the further upward shift of the bands relative to the pristine case, but the TSS

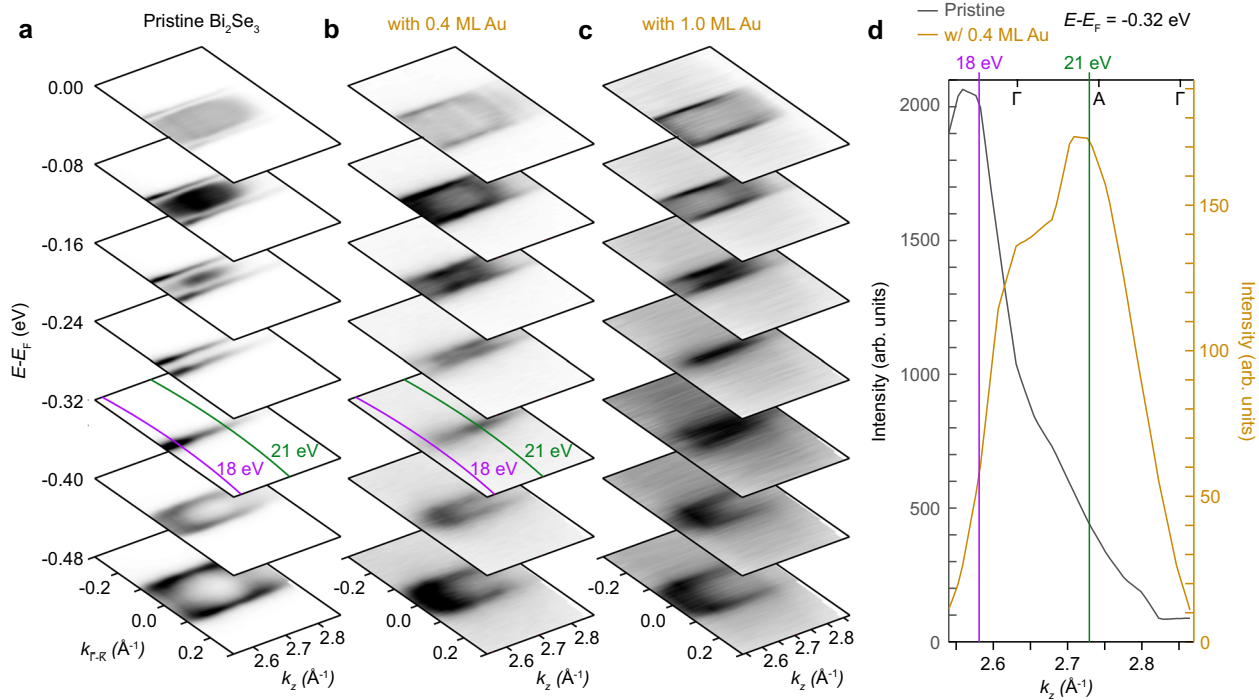


**Fig. 3 Photon-energy dependence of photoemission matrix elements.** **a–c** Constant energy  $k_x$ – $k_z$  contours for pristine and Au-dosed  $\text{Bi}_2\text{Se}_3$ . The green and purple lines in select contours highlight the  $k$ -vectors corresponding to  $h\nu = 18$  and 21 eV respectively, with which all dispersions shown in Fig. 2 are taken. The displayed  $k_z$  range spans over 1.5 complete Brillouin zones. **b, c** Equivalent dataset following 0.4 (**b**) and 1.0 (**c**) monolayers (ML) of Au deposition. **d** Out-of-plane ( $k_z$ ) momentum-distribution curve for  $k_x = 0 \text{ \AA}^{-1}$  and  $E - E_F = -0.32 \text{ eV}$  highlighting the suppression of Dirac point intensity for low photon energies following 0.4 ML Au deposition. High symmetry points, along with the  $k_z$  vectors corresponding to 18 and 21 eV photons, are indicated.

is always ungapped when observed with 21 eV photons. Figure 2g, h summarises the observed behavior of the Dirac point, with  $\bar{\Gamma}$ -point energy-distribution curves shown for each of the six experimental conditions considered. Again, the peak corresponding to the Dirac point vanishes for the 18 eV dataset (Fig. 2g), and instead shifts to shallower binding energy when observed with 21 eV photons (Fig. 2h).

As an aside, we note that the study presented by Polyakov et al.<sup>27</sup> demonstrates a gapped state following Au deposition for 21.2 eV photons, whereas here the surface state is observed to be ungapped for similar photon energy, but gapped for 18 eV photons. The altered experimental geometry between the studies, along with potentially differing light polarisations, are likely responsible for this discrepancy. The fact remains, however, that experimental conditions can be found such that the TSS is observed to be ungapped following large amounts of surface Au deposition, in contrast to the established literature.

### Modulation of photoemission matrix elements by gold

In Fig. 3, we further explore the photon-energy dependence of the photoemission matrix elements of the Dirac point in Au-dosed  $\text{Bi}_2\text{Se}_3$ . Figure 3a shows a series of constant energy  $k_x$ – $k_z$  contours for the three deposition levels already discussed, obtained by continuously varying the incident photon energy and assuming a free-electron-like final state<sup>39</sup>. In each case, diffuse spectral weight contributed by the bulk conduction and valence bands can be seen to disperse in  $k_z$ . In contrast, the sharp spectral weight of the TSS and SR states is entirely two-dimensional in line with their surface localisation, although the relative intensity of the bands varies significantly with photon energy. Focusing on the TSS, Fig. 3d shows momentum-distribution curves for the pristine and 0.4 ML surface doped sample, at the energy of the Dirac point. Following deposition, the peak of spectral weight clearly shifts and falls to near-zero in the lower  $h\nu$  region. This highlights the

strong photon-energy-dependent matrix elements for the TSS in Au-dosed  $\text{Bi}_2\text{Se}_3$ . This strong suppression of matrix elements could indeed be related to the formation of Au resonance states in the near- $E_F$  region (shown via density of states analyses in ref. <sup>27</sup>), leading to a change in the photon energy needed to favourably select the bands of the TSS from the background of superimposed Au states. Indeed, the Bi 6p and Se 4p orbitals, relevant for the  $\text{Bi}_2\text{Se}_3$  band inversion, have photoionisation cross-sections that decrease rapidly with increasing photon energy within the range shown in Fig. 3, with the opposite true for Au 5d orbitals<sup>42,43</sup>.

Next, we return to the discussion of the surface resonance states, which are by now well established to accompany the TSS<sup>29–31</sup>, and are seen in Fig. 2a, b. Following Au deposition (Fig. 2c–h), the signatures of the two surface resonance states become greatly enhanced relative to the pristine case, with the conduction band SR accumulating spectral weight around the full perimeter of the conduction band including at the  $\bar{\Gamma}$  point. These states were previously argued to be remnants of the gapped TSS<sup>27</sup>, and unrelated to the surface resonance states shown to exist in the pristine compound. However, this interpretation fails when changing the photon energy to  $h\nu = 21 \text{ eV}$ , where the spectral weight of the TSS, and its intact Dirac point recovers. The SR states therefore must be distinct from the TSS, and are most likely the same states as identified in the pristine compound. We will show that this indeed the case in Fig. 4.

### Spin-texture stability of surface states and resonances

Figure 4 again shows a dataset acquired with  $h\nu = 18 \text{ eV}$  photons before and after Au deposition. This dataset originates from a different sample to that shown in Figs. 2 and 3, with 1.0 ML of Au deposited on the surface in a single deposition step. The results are entirely consistent with those shown in Figs. 2–3, although we note that the conduction band SR is more clearly seen on this

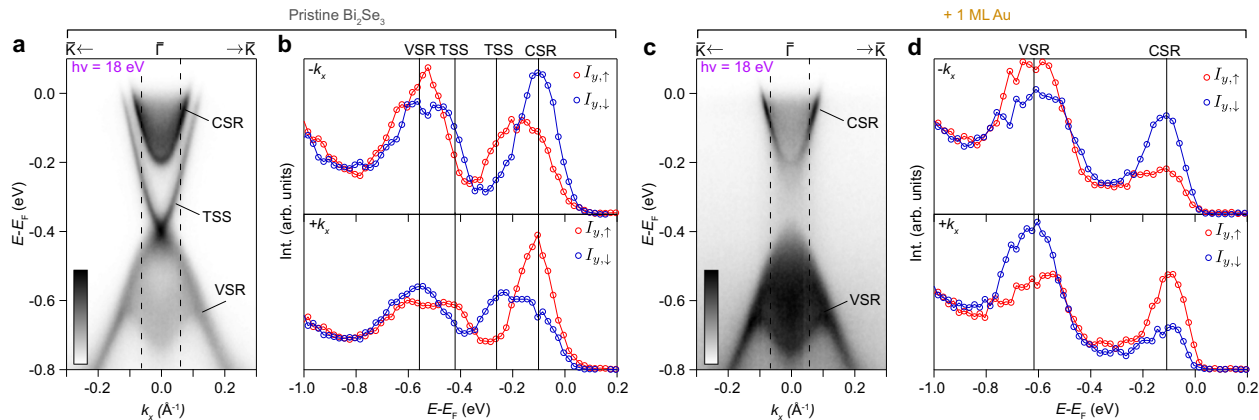


**Fig. 4 Robust spin texture of the topological surface state and surface resonances.** **a** Near- $E_F$  electronic structure of pristine  $\text{Bi}_2\text{Se}_3$ , as seen with 18 eV photons. The dashed lines indicate the momentum positions of the spin-resolved energy-distribution curves (EDCs) shown in **b**. **b** Spin-resolved EDCs for the in-plane chiral spin component ( $S_y$ ) (positions indicated in **a** through the conduction band surface resonance (CSR), valence band surface resonance (VSR) and the topological surface state (TSS). **c** Equivalent spectrum to that shown in **a**, but following Au deposition. Only the CSR and VSR states remain. The dashed lines indicate the momentum positions of the spin-resolved EDCs in **d**. **d** Spin-resolved EDCs through the TSS and the surface resonance states following 1.0 ML Au deposition, establishing that the chirality of the SR states is unchanged from that of the pristine sample. Colour scales for photoemission intensity run from low (white) to high (black).

second pristine sample, possibly enhanced in appearance by an additional  $n$  – doping originating from surface-layer Se vacancies<sup>41,44</sup>. For both experimental conditions, pairs of spin-resolved energy-distribution curves (spin-EDCs) are displayed at the indicated  $k$  points, for the perpendicular in-plane momentum direction (chiral component). This component should be dominant for any topological and Rashba surface state, even when accounting for warping originating from higher-order Rashba components<sup>45–47</sup>, coupled spin-orbital textures<sup>48,49</sup> or the influence of a dense  $k_z$  projected bulk band manifold<sup>50</sup>, and indeed this holds true for the  $\text{Bi}_2\text{Se}_3$  class of topological insulators<sup>30,51,52</sup>.

In the pristine sample (Fig. 4a),  $h\nu = 18 \text{ eV}$  is favourable for strong spectral weight for both the TSS and the surface resonance states, particularly the state following the perimeter of the bulk conduction band. The spin-resolved EDCs shown in Fig. 4b clearly demonstrate a relative up-down-up-down ordering for the conduction band surface resonance (CSR), the upper branch of the TSS, the lower branch of the TSS, and the valence band surface resonance (VSR), respectively. All four states switch sign from  $-k_x$  to  $+k_x$  in accordance with time-reversal symmetry. The absolute chiralities of both the TSS and SR states are entirely in line with previous theoretical and experimental studies<sup>29–31</sup>. We note, in particular, the opposite spin chiralities of the SR and TSS states<sup>29,30</sup>.

Figure 4c-d displays an equivalent dataset following Au deposition. The spectral weight of the surface resonance states remains strong, but, as shown in Fig. 2, the signatures of the TSS state vanish. Accordingly, the peaks in the spin-resolved EDCs corresponding to the TSS state in Fig. 4b are absent in Fig. 4d. The peaks corresponding to the SR states are qualitatively the same following Au deposition as they were previously. This observation is in excellent agreement with ref. <sup>27</sup>: An anti-clockwise chiral spin polarisation is measured in the conduction bands despite the apparent gapping of the TSS. However, the polarisation originates from the surface resonance states present even before Au deposition, not from a remnant gapped TSS. We note that any remnant states following a non-magnetic gapping of a Dirac point should have the same sense of chirality as the pristine TSS<sup>12,53</sup>, and not the opposite handedness clearly exhibited by the states observed here.

In conclusion, through a photon-energy-dependent spin- and angle-resolved photoemission study, we have shown that the spectral weight in  $\text{Bi}_2\text{Se}_3$  photoemission spectra is strongly photon-energy-dependent following Au deposition, and that the topological surface state of  $\text{Bi}_2\text{Se}_3$  can almost completely vanish for certain

choices of  $h\nu$ . However, this is a photoemission matrix element suppression, with signatures of the TSS and intact Dirac point recoverable with a change of photon energy. We conclude, therefore, that the topological surface state and accompanying surface resonance states in  $\text{Bi}_2\text{Se}_3$  are robust against high levels of surface Au deposition, in contrast to previous reports, and that there is not a mechanism by which Au impurity states lead to the hybridisation and subsequent gapping of the topological state that would be analogous to the Mn or In bulk doped  $\text{Bi}_2\text{Se}_3$  systems. The clarification provided here aids the effort towards a complete understanding of the effects of elemental incorporations on topological states within the Bi/Sb chalcogenide series. In addition, while such drastic changes of photoemission matrix elements are more likely to occur in studies where the sample surface is significantly altered (compared to the study of bulk doped systems, for example), this study outlines the need for variable photon-energy synchrotron and/or laser sources when drawing conclusions from the intensity of photoemission data in general.

## METHODS

We carried out ARPES experiments using  $p$ -polarised synchrotron light of energies between 17 and 120 eV under the experimental geometry shown in Fig. 1a. Photoelectrons were detected with a Scienta R4000 analyzer at the U125-2-PGM beamline of BESSY-II. The base pressure of the setup was  $\sim 1 \times 10^{-10} \text{ mbar}$ . The spin resolution was achieved using a Mott-type spin polarimeter operated at 25 kV. High-quality  $\text{Bi}_2\text{Se}_3$  single crystals were grown by the Bridgman method and cleaved in situ. The Au source was carefully calibrated using a quartz crystal monitor (QCM). Two samples were surface dosed at temperatures between 140 and 160 K. Sample 1 was measured in three conditions: Pristine, following 0.4 monolayers (ML) Au deposition and following a further 0.6 ML Au deposition (Figs. 2 and 3). Sample 2 was measured both pristine and following a single deposition of 1.0 ML Au (Figs. 1c and 4). For the photon-energy-dependent datasets in Fig. 3, a free-electron final state assumption was used with an inner potential,  $V_0$ , of 11.8 eV, in order to calculate  $k_z$  values from the corresponding photon energies<sup>39</sup>.

## DATA AVAILABILITY

The data that support the findings of this study are available from the corresponding author upon reasonable request.

Received: 8 November 2021; Accepted: 16 February 2022;  
Published online: 28 March 2022

## REFERENCES

1. Zhang, H. et al. Topological insulators in  $\text{Bi}_2\text{Se}_3$ ,  $\text{Bi}_2\text{Te}_3$  and  $\text{Sb}_2\text{Te}_3$  with a single Dirac cone on the surface. *Nat. Phys.* **5**, 438–442 (2009).
2. Kim, S. et al. Robust protection from backscattering in the topological insulator  $\text{Bi}_{1.5}\text{Sb}_{0.5}\text{Te}_{1.7}\text{Se}_{1.3}$ . *Phys. Rev. Lett.* **112**, 136802 (2014).
3. Valla, T., Pan, Z.-H., Gardner, D., Lee, Y.-S. & Chu, S. Photoemission spectroscopy of magnetic and nonmagnetic impurities on the surface of the  $\text{Bi}_2\text{Se}_3$  topological insulator. *Phys. Rev. Lett.* **108**, 117601 (2012).
4. Du, R. et al. Robustness of topological surface states against strong disorder observed in  $\text{Bi}_2\text{Te}_3$  nanotubes. *Phys. Rev. B* **93**, 195402 (2016).
5. Neupane, M. et al. Observation of quantum-tunnelling-modulated spin texture in ultrathin topological insulator  $\text{Bi}_2\text{Se}_3$  films. *Nat. Commun.* **5**, 3841 (2014).
6. Chen, Y. L. et al. Massive dirac fermion on the surface of a magnetically doped topological insulator. *Science* **329**, 659–662 (2010).
7. Xu, S.-Y. et al. Hedgehog spin texture and Berry's phase tuning in a magnetic topological insulator. *Nat. Phys.* **8**, 616–622 (2012).
8. Scholz, M. R. et al. Tolerance of topological surface states towards magnetic moments: Fe on  $\text{Bi}_2\text{Se}_3$ . *Phys. Rev. Lett.* **108**, 256810 (2012).
9. Scholz, M. R. et al. Intact dirac cone of  $\text{Bi}_2\text{Te}_3$  covered with a monolayer Fe. *Phys. Status Solidi Rapid Res. Lett.* **7**, 139–141 (2013).
10. Ye, M. et al. Quasiparticle interference on the surface of  $\text{Bi}_2\text{Se}_3$  induced by cobalt adatom in the absence of ferromagnetic ordering. *Phys. Rev. B* **85**, 205317 (2012).
11. Honokla, J. et al. In-plane magnetic anisotropy of Fe atoms on  $\text{Bi}_2\text{Se}_3(111)$ . *Phys. Rev. Lett.* **108**, 256811 (2012).
12. Sánchez-Barriga, J. et al. Nonmagnetic band gap at the Dirac point of the magnetic topological insulator  $(\text{Bi}_{1-x}\text{Mn}_x)_2\text{Se}_3$ . *Nat. Commun.* **7**, 10559 (2016).
13. Chang, C.-Z. et al. Chemical-potential-dependent gap opening at the dirac surface states of  $\text{Bi}_2\text{Se}_3$  induced by aggregated substitutional Cr atoms. *Phys. Rev. Lett.* **112**, 056801 (2014).
14. Black-Schaffer, A. M. & Balatsky, A. V. Strong potential impurities on the surface of a topological insulator. *Phys. Rev. B* **85**, 121103 (2012).
15. Black-Schaffer, A. M. & Balatsky, A. V. Subsurface impurities and vacancies in a three-dimensional topological insulator. *Phys. Rev. B* **86**, 115433 (2012).
16. Biswas, R. R. & Balatsky, A. V. Impurity-induced states on the surface of three-dimensional topological insulators. *Phys. Rev. B* **81**, 233405 (2010).
17. Brahlek, M. et al. Topological-metal to band-insulator transition in  $(\text{Bi}_{1-x}\text{In}_x)_2\text{Se}_3$  thin films. *Phys. Rev. Lett.* **109**, 186403 (2012).
18. Rienks, E. D. L. et al. Large magnetic gap at the Dirac point in  $\text{Bi}_2\text{Te}_3/\text{MnBi}_2\text{Te}_4$  heterostructures. *Nature* **576**, 423–428 (2019).
19. Lu, R. et al. Half-magnetic topological insulator with magnetization-induced dirac gap at a selected surface. *Phys. Rev. X* **11**, 011039 (2021).
20. Klimovskikh, I. I. et al. Tunable 3D/2D magnetism in the  $(\text{MnBi}_2\text{Te}_4)(\text{Bi}_2\text{Te}_3)_m$  topological insulators family. *npj Quantum Mater.* **5**, 54 (2020).
21. Trang, C. X. et al. Crossover from 2D ferromagnetic insulator to wide band gap quantum anomalous hall insulator in ultrathin  $\text{MnBi}_2\text{Te}_4$ . *ACS Nano* **15**, 13444–13452 (2021).
22. Voborník, I. et al. Observation of distinct bulk and surface chemical environments in a topological insulator under magnetic doping. *J. Phys. Chem. C* **118**, 12333–12339 (2014).
23. Sánchez-Barriga, J. et al. Anomalous behavior of the electronic structure of  $(\text{Bi}_{1-x}\text{In}_x)_2\text{Se}_3$  across the quantum phase transition from topological to trivial insulator. *Phys. Rev. B* **98**, 235110 (2018).
24. Růžička, J. et al. Structural and electronic properties of manganese-doped  $\text{Bi}_2\text{Te}_3$  epitaxial layers. *New J. Phys.* **17**, 013028 (2015).
25. Wimmer, S. et al. Mn-rich  $\text{MnSb}_2\text{Te}_4$ : a topological insulator with magnetic gap closing at high Curie temperatures of 45–50 K. *Adv. Mater.* **33**, 2102935 (2021).
26. Black-Schaffer, A. M., Balatsky, A. V. & Fransson, J. Filling of magnetic-impurity-induced gap in topological insulators by potential scattering. *Phys. Rev. B* **91**, 201411 (2015).
27. Polyakov, A. et al. Instability of the topological surface state in  $\text{Bi}_2\text{Se}_3$  upon deposition of gold. *Phys. Rev. B* **95**, 180202 (2017).
28. Polyakov, A. et al. Reply to "Comment on 'Instability of the topological surface state in  $\text{Bi}_2\text{Se}_3$  upon deposition of gold'". *Phys. Rev. B* **98**, 136202 (2018).
29. Cacho, C. et al. Momentum-resolved spin dynamics of bulk and surface excited states in the topological insulator  $\text{Bi}_2\text{Se}_3$ . *Phys. Rev. Lett.* **114**, 097401 (2015).
30. Jozwiak, C. et al. Spin-polarized surface resonances accompanying topological surface state formation. *Nat. Commun.* **7**, 13143 (2016).
31. Sánchez-Barriga, J. et al. Subpicosecond spin dynamics of excited states in the topological insulator  $\text{Bi}_2\text{Te}_3$ . *Phys. Rev. B* **95**, 125405 (2017).
32. Dunlap, W. C. Gold as an acceptor in germanium. *Phys. Rev.* **97**, 614–629 (1955).
33. Bahramy, M. S. et al. Emergent quantum confinement at topological insulator surfaces. *Nat. Commun.* **3**, 1159 (2012).
34. Sakano, M. et al. Strongly spin-orbit coupled two-dimensional electron gas emerging near the surface of polar semiconductors. *Phys. Rev. Lett.* **110**, 107204 (2013).
35. King, P. D. C. et al. Surface band-gap narrowing in quantized electron accumulation layers. *Phys. Rev. Lett.* **104**, 256803 (2010).
36. Mazzola, F. et al. Simultaneous conduction and valence band quantization in ultrashallow high-density doping profiles in semiconductors. *Phys. Rev. Lett.* **120**, 046403 (2018).
37. Clark, O. J. et al. Dual quantum confinement and anisotropic spin splitting in the multivalley semimetal  $\text{PtSe}_2$ . *Phys. Rev. B* **99**, 045438 (2019).
38. Gordon, R. A. Comment on "Instability of the topological surface state in  $\text{Bi}_2\text{Se}_3$  upon deposition of gold". *Phys. Rev. B* **98**, 136201 (2018).
39. Damascelli, A. Probing the electronic structure of complex systems by ARPES. *Phys. Scripta* **2004**, T109 61 (2004).
40. Seibel, C. et al. Connection of a topological surface state with the bulk continuum in  $\text{Sb}_2\text{Te}_3(0001)$ . *Phys. Rev. Lett.* **114**, 066802 (2015).
41. Bianchi, M. et al. Coexistence of the topological state and a two-dimensional electron gas on the surface of  $\text{Bi}_2\text{Se}_3$ . *Nat. Commun.* **1**, 128 (2010).
42. Parry, D. E. Atomic calculation of photoionization cross-sections and asymmetry parameters. *Rapid Commun. Mass Spectrom.* **8**, 579–579 (1994).
43. Yeh, J. J. & Lindau, I. Atomic subshell photoionization cross sections and asymmetry parameters:  $1 \leq Z \leq 103$ . *At. Data Nucl. Data Tables* **32**, 1–155 (1985).
44. Hor, Y. S. et al. p-type  $\text{Bi}_2\text{Se}_3$  for topological insulator and low-temperature thermoelectric applications. *Phys. Rev. B* **79**, 195208 (2009).
45. Fu, L. Hexagonal warping effects in the surface states of the topological insulator  $\text{Bi}_2\text{Te}_3$ . *Phys. Rev. Lett.* **103**, 266801 (2009).
46. Michiardi, M. et al. Strongly anisotropic spin-orbit splitting in a two-dimensional electron gas. *Phys. Rev. B* **91**, 035445 (2015).
47. Akzyanov, R. S. & Rakhmanov, A. L. Bulk and surface spin conductivity in topological insulators with hexagonal warping. *Phys. Rev. B* **99**, 045436 (2019).
48. Zhang, H., Liu, C.-X. & Zhang, S.-C. Spin-orbital texture in topological insulators. *Phys. Rev. Lett.* **111**, 066801 (2013).
49. Bawden, L. et al. Hierarchical spin-orbital polarization of a giant Rashba system. *Sci. Adv.* **1**, 1500495 (2015).
50. Clark, O. J. et al. A general route to form topologically-protected surface and bulk Dirac fermions along high-symmetry lines. *Electron. Struct.* **1**, 014002 (2019).
51. Souma, S. et al. Direct measurement of the out-of-plane spin texture in the dirac-cone surface state of a topological insulator. *Phys. Rev. Lett.* **106**, 216803 (2011).
52. Sánchez-Barriga, J. et al. Photoemission of  $\text{Bi}_2\text{Se}_3$  with circularly polarized light: probe of spin polarization or means for spin manipulation? *Phys. Rev. X* **4**, 011046 (2014).
53. Xu, S.-Y. et al. Unconventional transformation of spin Dirac phase across a topological quantum phase transition. *Nat. Commun.* **6**, 6870 (2015).

## ACKNOWLEDGEMENTS

J.S.-B. acknowledges financial support from the Impuls- und Vernetzungsfonds der Helmholtz-Gemeinschaft under grant No. HRSF-0067.

## AUTHOR CONTRIBUTIONS

O.J.C. and J.S.-B. prepared the manuscript with input from O.R. and L.V.Y. O.J.C., F.F. and J.S.-B. performed the experiment. L.V.Y. provided samples. J.S.-B. was responsible for overall project planning and direction.

## FUNDING

Open Access funding enabled and organized by Projekt DEAL.

## COMPETING INTERESTS

The authors declare no competing interests.

## ADDITIONAL INFORMATION

**Correspondence** and requests for materials should be addressed to J. Sánchez-Barriga.

**Reprints and permission information** is available at <http://www.nature.com/reprints>

**Publisher's note** Springer Nature remains neutral with regard to jurisdictional claims in published maps and institutional affiliations.



**Open Access** This article is licensed under a Creative Commons Attribution 4.0 International License, which permits use, sharing, adaptation, distribution and reproduction in any medium or format, as long as you give appropriate credit to the original author(s) and the source, provide a link to the Creative Commons license, and indicate if changes were made. The images or other third party material in this article are included in the article's Creative Commons license, unless indicated otherwise in a credit line to the material. If material is not included in the article's Creative Commons license and your intended use is not permitted by statutory regulation or exceeds the permitted use, you will need to obtain permission directly from the copyright holder. To view a copy of this license, visit <http://creativecommons.org/licenses/by/4.0/>.

© The Author(s) 2022